Materials Science & Engineering A 839 (2022) 142831

Contents lists available at ScienceDirect

Materials Science & Engineering A

journal homepage: www.elsevier.com/locate/msea

Impact loading of functionally graded metal syntactic foams

Nima Movahedi [a], Thomas Fiedler [a,*], Alper Taşdemirci [b], Graeme E. Murch [a], Irina V. Belova [a], Mustafa Güden [b]

[a] Centre for Mass and Thermal Transport in Engineering Materials, College of Engineering, Science and Environment, The University of Newcastle, Callaghan, NSW, Australia

[b] Dynamic Testing and Modeling Laboratory and Department of Mechanical Engineering, Izmir Institute of Technology, Gülbahçe Köyü, Urla, Izmir, Turkey

ARTICLE INFO

Keywords:
Functionally graded metal syntactic foam
Impact loading
Mechanical properties
Deformation mechanism

ABSTRACT

The present study addresses the impact loading of functionally graded metal syntactic foams (FG-MSF). For comparison, samples of the same material were also compression loaded at quasi-static velocities. Samples of A356 aluminium FG-MSF were produced using counter-gravity infiltration casting with combination of equal-sized layers of expanded perlite (EP) and activated carbon (AC) particles. A modified Split Hopkinson Pressure Bar test set-up was used to impact the FG-MSFs from their EP or AC layers at 55 m/s or 175 m/s impact velocities. A high-speed camera captured the deformation of the samples during testing. It was shown that increasing the loading velocity enhanced both the compressive proof strength and energy absorption of the impacted FG-MSF from both layers, confirming a dynamic strengthening effect of the foam. The samples impacted from both layers at 55 and 175 m/s showed a transition and a shock mode of deformation, respectively. The impacted samples at 55 m/s experienced lower final average strain values compared to 175 m/s.

1. Introduction

The porous structure of metallic foams makes them suitable in applications involving impact energy mitigation, for example, the bumpers of automobiles which absorb the impact energy of accidents [1–3]. For that, the mechanical behaviours of metal foams have been widely investigated at high strain rates [4–6]. The mechanical response at increasing strain rates has been shown to change significantly compared to quasi-static loadings [7]. Both the strain rate sensitivity of the metal from which the foam is made and the micro-inertia affect the mechanical response at high strain rates [8]. Although, the cell wall buckling was shown to be the dominant deformation mode under quasi-static loading [9], this mode is restricted by the cell-wall inertia at high strain rates. Above a critical velocity, the cellular structure deforms by forming sequential, planar crush bands propagating from the impact-end, which is known as shock stress. This deformation mode provides an additional strengthening at high velocities [10]. The dynamic compressive properties of closed-cell aluminium foams with different cell sizes were experimentally investigated using a direct impact test at different velocities between 10 − 210 m/s [10]. Beyond the critical velocity value of 100 m/s, the dynamic strengthening of the aluminium foam was observed due to the inertial effect associated with the dynamic localisation of the crushing. It was shown in Ref. [10] that at velocity regime higher than 100 m/s, any effect of cell size or morphological defects is insignificant. Therefore, a strong effect of cell dimension is not expected for the investigated syntactic foams.

Vesenjak et al. [11] investigated the strengthening of an open-cell aluminium foam at high strain rates under compression. Their numerical study showed that above 100 s^{-1}, the effect of strain rate sensitivity of matrix outweighs the effect of micro-inertia. Güden and Canbaz [12] investigated the strain rate hardening of a layered 1050 H14 aluminium corrugated structure both experimentally and numerically through a direct impact test method. It was shown that the initial peak stress of a low strain rate hardening aluminium alloy was mostly influenced by micro-inertia. The shock deformation mode was also observed above a critical loading velocity. Fiedler et al. [13] investigated the dynamic compression of an A356 aluminium alloy-expanded perlite syntactic foam. Compared to quasi-static compression, the strength of the MSF showed an increase at higher strain rates due to the strain rate sensitivity of the A356 aluminium alloy. In Ref. [14] it was shown that under dynamic loading the strength of the A356 aluminium alloy and its composites are enhanced by the strain rate hardening effect. In addition, the entrapped air within expanded perlite (EP) particles in MSFs in Ref. [13] was suspected to build up a pressure within the EP particles during

* Corresponding author.
E-mail address: Thomas.Fiedler@newcastle.edu.au (T. Fiedler).

https://doi.org/10.1016/j.msea.2022.142831
Received 14 October 2021; Received in revised form 9 February 2022; Accepted 12 February 2022
Available online 15 February 2022

compression that stabilize the adjacent cell walls.

In another study [15], a chiral auxetic cellular structure made of copper and manufactured by Selective Electron Beam Melting was investigated under quasi-static and high strain rate compression. At high loading velocities, the shock deformation mode was observed; the plateau stress increased with increasing the loading velocity. Movahedi et al. [16] studied the dynamic compression of a FG-MSF using ZA27 matrix alloy with layered arrangements of EP and activated carbon (AC) fillers. Regardless of the loading direction, the dynamic compression of the FG-MSF started at the lowest density layer (EP layer) of the material. In another study [17], the dynamic compression of a functionally graded metal hollow sphere was numerically investigated. The gradient was introduced using similar hollow metal spheres with different wall thickness along the longitudinal direction of the material. The deformation started at the impact region in high velocity impact tests. The energy absorption of the graded foam model showed better results when the higher density layer was impacted first.

He et al. [18] manufactured density-graded closed-cell aluminium foams using a modified casting technique. Compared to their uniform samples, the impact of these graded aluminium foams resulted in lower initial compressive strength due to the lowest local density at the impinging end. Further compression of the graded foam resulted in a higher stress compared to uniform samples. This provided a more extended plateau region for the graded closed-cell aluminium foams under impact loading.

A Voronoi 3D foam model was used to numerically investigate the impact properties of a graded metal foam in Ref. [19]. The gradation was achieved by changing the relative density within the model. By tailoring the gradation configuration, the dynamic compression of the model was studied. The results showed the maximum energy absorption at low strains when the negative gradation model was adopted. While the positive gradation was preferred for energy absorption at high strains.

The present research study investigates the impact loading of FG-MSF with an A356 aluminium matrix and layered arrangements of EP and AC porous particles. The influence of the loading direction and the loading velocity on the stress-strain response, mechanical properties, and the deformation mechanism of the FG-MSF are studied. The results of the impact loading tests are further compared to those of the quasi-static loading tests.

2. Materials and methods

2.1. Manufacture of FG-MSF

Counter gravity infiltration casting was used to manufacture layered FG-MSF samples. A356 aluminium alloy and porous EP and AC particles were used as the matrix and filler particles, respectively. A similar procedure is described for a ZA27 alloy matrix in Ref. [20]. Utilizing two dissimilar types of porous particles with different physical and mechanical properties is a relatively novel technique to manufacture MSFs with a strong gradient in their physical and mechanical properties [20]. This approach was used successfully to control the mechanical properties of the FG-MSFs under quasi-static, dynamic and fatigue loadings [16,21]. Alternatively, FG-MSFs can be manufactured using different volume fraction and a single type of filler particle (EP) [22]. In this study, dissimilar particles were selected because this approach enables larger differences in the mechanical properties of individual layers.

The volume of the mould was evenly divided between the particle types. The first sub-volume was filled with AC particles. The partially

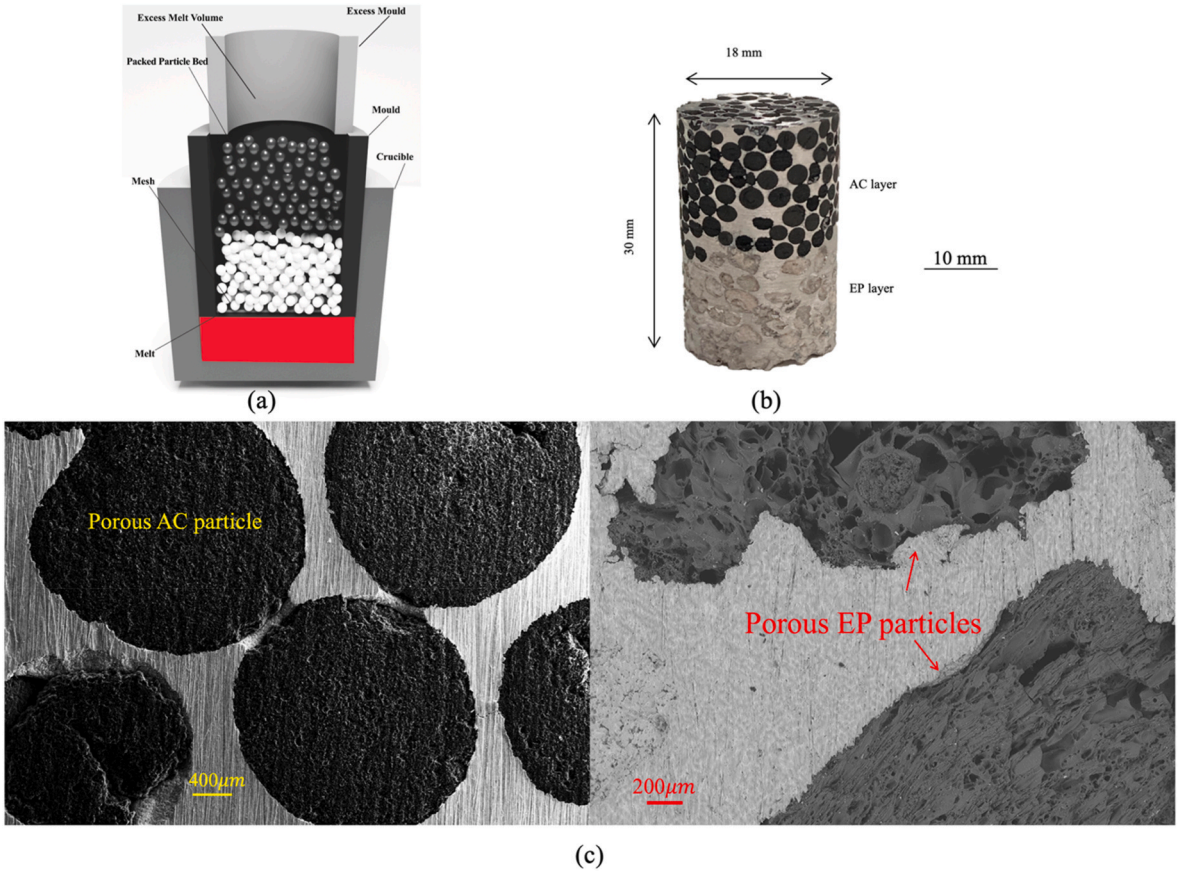

Fig. 1. (a) Schematic of infiltration casting, (b) a cast A356 FG-MSF sample and (c) the SEM images of each layer with porous AC and EP particles inside the matrix alloy.

filled mould was tapped and vibrated to achieve a homogeneous packing of AC particles. A paper membrane was placed on the top of AC filler to separate it from the next layer. The remainder of the mould was then filled with EP particles, again with tapping and vibration (see Fig. 1a). A steel mesh was placed on the top of the particles to keep them in place during subsequent handling. A piece of solid A356 aluminium alloy was inserted within a graphite crucible. Then, the rotated graphite mould was inserted on top the metal piece into the graphite crucible. The resulting assembly was heated in an electrical furnace at 720 °C for 30 min within a protective argon atmosphere to minimize the oxidation of the matrix. According to an established procedure [13], this temperature forms a compromise to achieve good infiltration of the matrix alloy into the packed beds of the particles but also minimize oxidation of the graphite crucibles.

The casting was completed by placing a 2 kg weight on top of the excess mould (see Fig. 1a) to push the mould downwards and infiltrate the molten alloy between the particles. Following solidification, samples were manually removed and machined into the dimension of ~30 mm in height and ≈ 18 mm in diameter (see Fig. 1b). Fig. 1 c shows the SEM images of the layers containing porous AC and EP particles. Porous AC particles exhibit a higher density which results in a lower pore volume fraction compared to the EP particles.

2.2. Physical properties of FG-MSF

The layer volume fraction ($\varnothing_i$) is defined as:

$$\varnothing_i = \frac{V_i}{\sum V_j} \tag{1}$$

where V_i is the volume of ith layer. In the two-layered FG-MSF considered, the volume fraction of each layer is assumed to be 0.5. The packing densities of particle beds ($\varnothing_P$) were determined previously [20] and found to be $\varnothing_{P,EP} = 56.88\%$ and $\varnothing_{P,AC} = 59.04\%$, respectively. Accordingly, the particle volume fraction in the layered FG-MSF is estimated as:

$$\varnothing_P = \sum \varnothing_{P,i}\varnothing_i \approx 0.5\ \varnothing_{P,EP} + 0.5\ \varnothing_{P,AC} \approx 57.96\% \tag{2}$$

In equation (2), 0.5 is related to the *volume fraction of each layer* in the structure of the FG-MSFs (see equation (1)). As described earlier, the casting mould was divided into two equal volumes in the longitudinal direction (see Fig.1a). Then, each section was filled with either porous AC or EP particles. In equation (2), $\varnothing_{P,EP}$ and $\varnothing_{P,AC}$ are the volume fraction of porous EP and AC particles in each layer of the FG-MSFs respectively. *The volume fraction of a particle in each layer* $\varnothing_{P,i}$ is considered equation (3) [20]:

$$\varnothing_{P,i} = \frac{\rho_B}{\rho_P} \tag{3}$$

Where ρ_B and ρ_P are the bulk and envelope density of the porous particles in each layer [20].

The particle mass (m_p) in FG-MSF is calculated using the following relation:

$$m_p = \sum \left(V_i\ \varnothing_{P,i}\ \rho_{P,i}\right) \tag{4}$$

The particle densities of EP ($\rho_{P,EP}$) and AC ($\rho_{P,AC}$) are 0.16 g / cm^3 and 0.83 g / cm^3 respectively [20] (the higher porosity of EP particles can be seen in Fig. 1c). Using the particle mass, the matrix volume fraction ($\varnothing_M$) can be calculated according to

$$\varnothing_M = \frac{m_{SF} - m_P}{V_{SF}\cdot\rho_M} \tag{5}$$

where $\rho_M = 2.68$ g/ cm^3 is the density of the A356 aluminium matrix alloy [23], m_{SF} is the syntactic foam mass and V_{SF} is the cylindrical syntactic foam volume. The overall volume fraction of the constituents in the structure of the material must be unity and therefore the volume fraction of the voids can be obtained from

$$\varnothing_M + \varnothing_P + \varnothing_V = 1 \tag{6}$$

2.3. Mechanical tests

Quasi-static compressions tests were performed in a 50 kN SHIMADZU test machine at a crosshead velocity of 16×10^{-4} m/s. Prior to compression testing, both contact surfaces of the samples were lubricated using a CRC® 5–56 multipurpose lubricant (CRC Industries, NSW, Australia) to minimize the friction with the compression test platens. Measured load-displacement values were converted into engineering stress (σ) and engineering strain (ε), respectively. Light photography was used to capture the deformation of the FG-MSF during compression.

Cylindrical FG-MSF samples were directly impacted using a modified Split Hopkinson Pressure Bar (SHPB) set-up having a 19.40 mm-diameter and 2480 mm-long Inconel 718 incident bar. The set-up is schematically shown in Fig. 2. The test samples were inserted inside the SHPB gas barrel (striker bar was removed). The specimen was fired by the gas gun to the end of a 19.40 mm diameter and 2480 mm long Inconel 718 Split Hopkinson Pressure Bar (SHPB) set-up. The velocity of the specimen was set using the pressure of the gas within the barrel. In the impact tests, the cylindrical FG-MSFs samples were directly impinged with the desired initial velocity of either 55 or 175 m/s. The applied impact tests in this study are very similar to the Taylor impact test setup [24] and the corresponding bar is named as incident bar for this configuration. This type of impact test is a non-equilibrium test to investigate the development of shock stress in cellular materials. This model was developed by Reid and Peng in 1997 [25] and yields the impact-end stress as a function of time.

The impact velocity was controlled by changing the gas gun pressure of the SHPB. Test samples were oriented to the impact alternatively with their AC or EP layers at two different impact velocities, 55 m/s and 175 m/s. The velocity of the samples is captured by the velocity measurement sensor inserted at the end of the gas barrel immediately before their impact to the incident bar (see Fig. 2). The captured velocities showed the values of 55 and 175 m/s for the impact of the samples in this study.

When the FG-MSF sample impacts the incident bar, a compressive wave forms on the incident bar. This wave was measured using three full-bridge strain gages mounted at three specific locations on the incident bar in conjunction with an amplifier and oscilloscope as shown in Fig. 2. A laser gate was used to measure the impact velocity. The use of three strain gauges allowed to monitor wave dispersion on the bar and to introduce redundancy in the case of sensor failure. The voltage readings of the oscilloscope were converted into strain measurements of the incident bar $\varepsilon_I(t)$ using the full-bridge strain gage circuit equation [26]:

$$\varepsilon_I(t) = \frac{2\int \varepsilon(V)dt}{G\cdot K\cdot V\ (1+\nu)} \tag{7}$$

where $\varepsilon(V)$ is the voltage read by the full-bridge strain gauges, G is the strain gauge amplifier gain (20), K is the strain gauge factor (2.09), V is the excitation voltage of the strain gauge bridge (10 V) and ν is the Poisson's ratio of the bar material (0.33 for Inconel 718 alloy). The stress in the sample $\sigma_s(t)$ is calculated as [26,27]:

$$\sigma_s(t) = \frac{A_b E \varepsilon_I}{A_s} \tag{8}$$

where A_b and A_s are the cross-sectional areas of bar and sample, respectively and E is the elastic modulus of the incident bar (210 GPa for Inconel 718 alloy). The diameter of the incident bar and the diameter of compression test sample were 19.40 and 0 18.00 mm respectively.

The FG-MSF sample's *average* strain was estimated using the following procedure. A high-speed imaging method is used to calculate

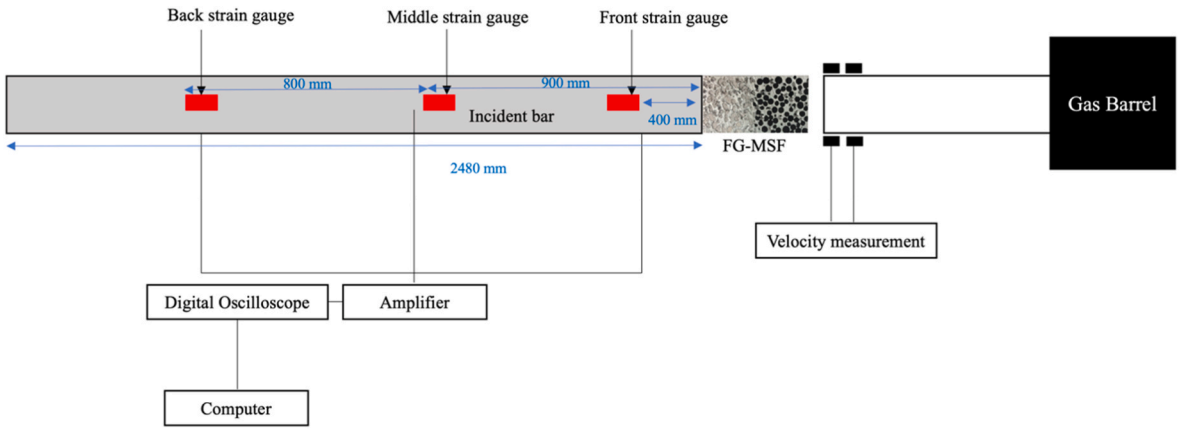

Fig. 2. The schematic of modified SHPB impact test setup.

the **average** strain in the FG-MSFs during their impact. This approach enables to calculate the **average** strain of the samples at different time intervals but not the local strain of each layer or within sections of the material. To this end, a Fastcam Photron high-speed camera captured the impact deformation of the sample at 100,000 frames per second. Images at 0, 20, 40 and 80 μs post impact were selected to calculate the average sample strain using the *ImageJ* software [28]. Sample deformation occurs within 80 μs after impacting the incident bar (see Fig. 4b). Therefore, this time interval was selected to calculate their average strain and capture macroscopic deformation.

To this end, the initial height of the samples ($L_0 \approx 30$ mm) was expressed in pixels based on the reference image at 0 μs. At subsequent time intervals, the sample's length (L) was measured (again in pixels) to calculate the average strains according to:

$$\varepsilon = \frac{L - L_0}{L_0} \tag{9}$$

For each test condition (impact velocity and impact direction), the average strain ε could thus be expressed as a function of the time t:

$$\varepsilon = f(t) \tag{10}$$

Synchronisation with the sample stress $\sigma_s(t)$ yielded the stress-strain curves of the FG-MSF. This stress-strain was then used to calculate mechanical properties following ISO 13314-2011 [29]. The compressive proof strength corresponds to 1% of plastic average strain and the plateau stress (σ_{Pl}) was calculated as the average stress between 20 and 40% of macroscopic strain. The energy absorption of the FG-MSF (W) was calculated up to 50% of average strain (see Eq. (11)) and the energy absorption efficiency (η) was obtained using Eq. (12) [29].

$$W = \int_0^{0.5} \sigma \, d\varepsilon \tag{11}$$

$$\eta = \frac{W}{\sigma_{max} \cdot 0.5} \tag{12}$$

2.4. Rigid-perfectly-plastic-locking (r-p-p-l) model

The r-p-p-l shock model was developed by Reid and Peng [25] to describe the enhancement in crushing strength of wood specimens. This

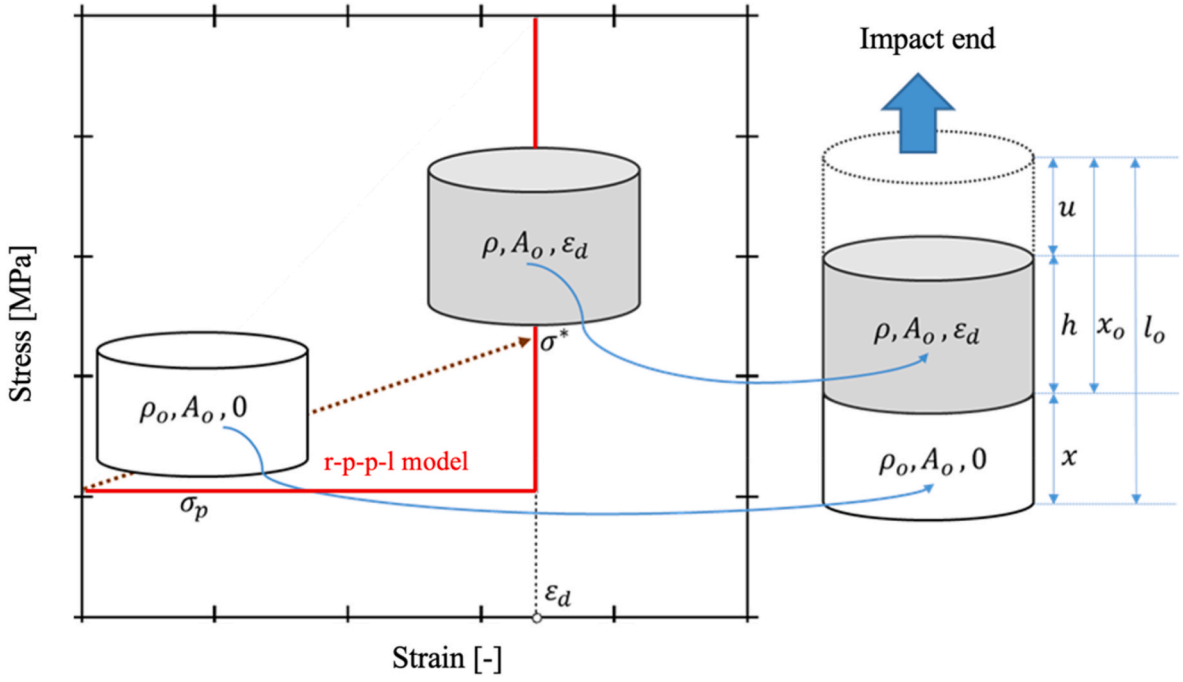

Fig. 3. Schematic of a uniform foam impact to a rigid wall: stress-strain curve and the deformed shape of foam sample.

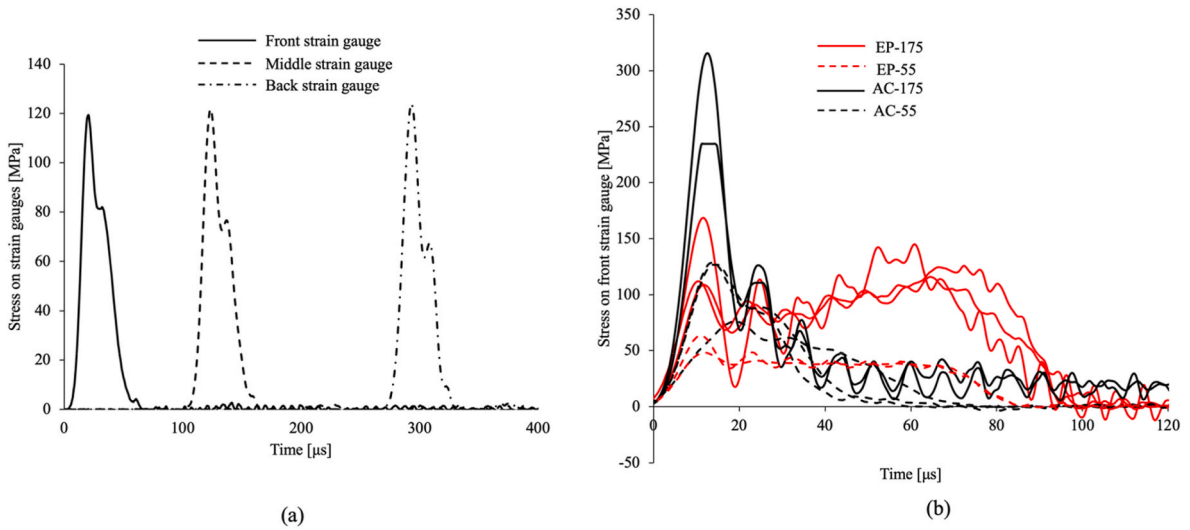

Fig. 4. The history of transmitted stress wave on the incident bar captured by three full-bridge strain gauges when the FG-MSF sample (a) impacted AC-55 sample 1, (b) front strain gauge stress-time history for samples impacted from different layers at different loading velocities.

model was then extended for metallic foams by Tan et al. [30] to predict the magnitude of their stress enhancement due to shock during impact. Shock enhancement is often used to explain the strength increase of the material at high strain rates [31,32]. The r-p-p-l model predicts merely the shock stresses [12]. To this end, the variation of stress over time is calculated using the following procedure: The impact of a uniform cellular material on a rigid wall with an initial velocity of v_o induces two distinct deformation regions: a crushed (densified) region with a stress of σ^* (initial crushing stress) and the elastically deformed region as seen in Fig. 3. The plateau stress of the cellular metal is considered as σ_P . In Fig. 3, u is the displacement, h is the length of the densified region, x is the uncrushed length, x_o is the initial length of the crushed region, ρ is the density of the crushed region, ρ_o is the initial density, l_o is the initial length, ε_d is the densification strain, and v_o is the initial velocity. The following relation applies to the initial and crushed section density as [24]:

$$\rho_o = \rho(1-\varepsilon_d) \tag{13}$$

The initial crushing stress can be determined by applying mass and momentum conservations between crushed and uncrushed section and Newton's second law to the uncrushed section give the crushing stress as [24]:

$$\sigma^*(t) = \sigma_p + \frac{\rho_o}{\varepsilon_d} v(t)^2 \tag{14}$$

where $v(t)$ is the velocity of the sample. The variation of velocity with time can be determined by applying Newton's second law to the uncrushed section [24]:

$$v(t) = \sqrt{v_o^2 + \frac{2\sigma_p \varepsilon_d}{\rho_o} ln\left(1 - \frac{\rho_o A_o u}{\varepsilon_d}\right)} \tag{15}$$

Inserting Eq. (14) into Eq. (13) yields the crushing stress as a time-dependent function [24]:

$$\sigma^*(t) = \sigma_p + \frac{\rho_o}{\varepsilon_d}\left[v_o^2 + \frac{2\sigma_p \varepsilon_d}{\rho_o} ln\left(1 - \frac{\rho_o A_o u}{\varepsilon_d}\right)\right] \tag{16}$$

The **initial** average strain rate was measured by dividing the impact velocity with the initial height of the FG-MSFs as the following equation:

$$\text{Strain rate} = \frac{V_0}{L_0} \tag{17}$$

In this equation, V_0 is the sample's velocity and L_0 is the sample's height. According to this equation, the corresponding initial average strain rates for the impacted samples at 55 m/s and 175 m/s are 1833 s^{-1} and 5833 s^{-1} respectively. (The samples initial height is about 30 mm, see Table 1).

3. Results and discussion

3.1. Physical properties

The physical properties of the FG-MSF samples are tabulated in Table 1. Henceforth, the samples are named according to their impacted layer and velocity as EP-55, EP-175, AC-55 and AC-175. For instance, EP-55 is the sample impacted from its EP layer at 55 m/s. The mechanical properties of metallic foams under compressive loading strongly depend on their density [1]. To minimize the effect of density in the present study, tested FG-MSF samples were selected from the narrow density range 1.36 to 1.41 g / cm^3 (see Table 1). The volume fractions of particles ($\varnothing_P$) is assumed to be identical in all samples (see Eq. (2)); hence, the matrix volume fraction $\varnothing_M$ becomes a function of the sample density. In Table 1, minor deviations of the matrix volume fraction $\varnothing_M$ can be observed. This is most likely due to the different levels of melt infiltration into the thin channels between adjacent particles during casting. The same effect results in a slightly increased void volume fraction.

3.2. Stress-time history

The stress-time history of sample AC-55 (sample 1) captured by the three strain gauges is shown in Fig. 4a. The three strain gauges read almost identical stress levels only offset by propagation time. This indicates a negligible wave dispersion within the Inconel 718 incident bar. This stress consistency was observed for all tested samples and therefore only the data of the front strain gauges are considered in the following. The stress-time histories of the samples tested at 55 m/s and 175 m/s are shown in Fig. 4b. The compressive stress and the arrest time (the time at which stresses become zero) increases with the impact velocity. This trend is independent of the layer facing the impact bar. Impact from the AC layer results in an increased arrest time at 175 m/s. In Fig. 4b, a sharp decline in stress is visible for both AC-55 and AC-175 samples. The plateau stress in these two groups is not significant. For the EP-55 and EP-175 samples, the plateau stress is more pronounced, which is most likely due to higher ductility of the EP layer. It was previously shown that EP particles due to their considerably low strength (high porosity)

Table 1
Physical properties of the A356 FG-MSF samples used in impact loading.

	Sample	Mass (g)	Diameter (mm)	Height (mm)	Density (g/cm^3)	m_P (g)	$\varnothing_M$%	$\varnothing_P$%	$\varnothing_V$%
AC-55	1	10.78	17.98	30.03	1.41	2.24	41.99	57.96	0.05
	2	10.77	18.00	30.03	1.41	2.24	41.81	57.96	0.23
	3	10.58	18.00	30.02	1.39	2.23	40.93	57.96	1.11
AC-175	4	10.53	18.00	30.02	1.36	2.29	40.39	57.96	1.65
	5	10.59	18.10	30.01	1.37	2.28	40.33	57.96	1.71
EP- 55	1	10.80	18.00	30.22	1.41	2.23	41.76	57.96	0.28
	2	10.78	18.01	30.05	1.41	2.25	41.79	57.96	0.25
EP-175	3	10.59	17.90	30.04	1.38	2.22	41.50	57.96	0.54
	4	10.68	17.90	30.31	1.39	2.24	41.45	57.96	0.59
	5	10.68	18.00	30.00	1.40	2.22	41.53	57.96	0.51

[20] do not contribute significantly to the stiffness of MSFs (see Fig. 1c). In contrast, AC fillers exhibit a higher density (see Fig. 1c) with significant strength that promote macroscopic shear failure of MSF. The higher initial crushing stress of the samples of AC impact side is therefore attributed to the higher strength of the AC layer, as previously reported in Ref. [20]. At least two tests were performed for each test configuration (see Table 1). At each initial average strain rate and impact end, the FG-MSF samples showed near similar behaviour (see Figs. 4b and 5).

3.3. Stress-strain data

The compressive stress-strain curves of the FG-MSF samples at quasi-static and dynamic velocities are shown in Fig. 5. The quasi-static curves exhibit three distinct regions (see Fig. 5). In the first region, the deformation is predominantly elastic, and both the EP and the AC layer are deformed. The second part of deformation that is known as the plateau region is due to layer-by-layer compression of EP layer until $\varepsilon \approx 0.3$. After partial densification of the EP layer, the sample fails by shearing of the AC section visible by the formation of multiple shear bands (see Fig. 6). In this stage the stress declines is obvious in Fig. 5 (see Quasi-static curves at $\varepsilon \approx 0.3$). In the final deformation stage at $\varepsilon \approx 0.8$, the compressed EP layer and sheared AC layer are densified together (see arrow at $\varepsilon \approx 0.8$ in Fig. 5). A similar sequential deformation mode was also observed in six-layered FG-MSF in Ref. [33]. In low velocity compression such as quasi-static tests, the inertial effect is negligible. In this case, deformation of the cellular material starts from its weakest section (in this case the EP layer) and then progresses towards the higher strength part of the material [20]. In this mode, changing the loading direction does not influence the sequential deformation of the material.

For dynamic loading and regardless of the impact side, the initial strength of FG-MSF is higher compared to quasi-statically compressed samples (see Fig. 5). This indicates dynamic strengthening of A356 FG-MSF. Dynamic strengthening of porous metals is attributed to the intrinsic strain rate sensitivity of the matrix alloy, micro-inertial effects and gas pressure built up in the EP particles during dynamic loading [13]. However, it is difficult to quantify the contribution of each parameter on the dynamic stress-strain curves. The micro-inertial effect and shock enhancement were shown to become significant at strain rates $> 2500\ s^{-1}$ [34,35]. In the present study, this initial average strain rate

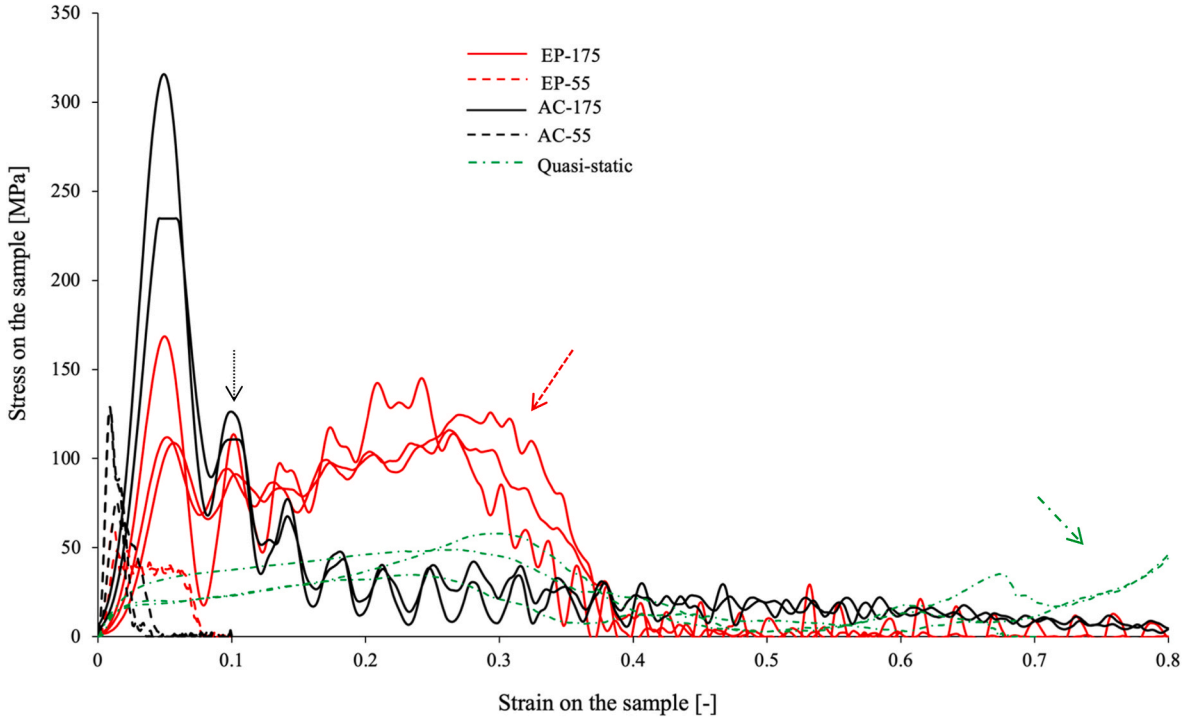

Fig. 5. Stress-strain curves of A356 FG-MSF samples under impact and quasi-static compression loadings.

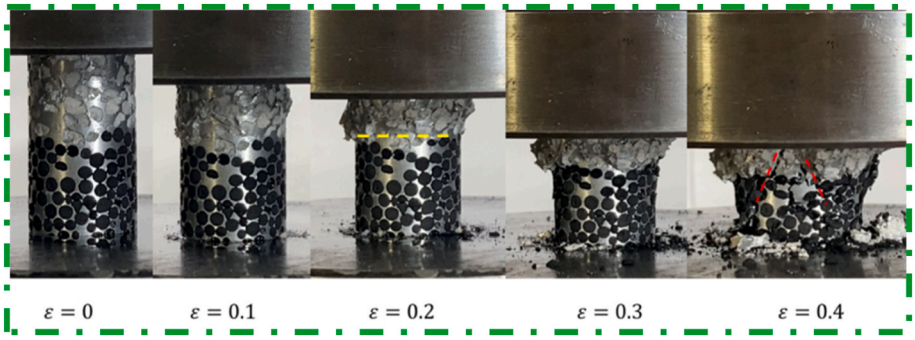

Fig. 6. Deformation of an A356 FG-MSF under quasi-static loading.

limit is exceeded by the impact velocity of 175 m/s (5833 s^{-1}), while a slightly lower initial average strain rate is obtained for the samples tested at 55 m/s (1833 s^{-1}). The deformation behaviour of cellular metals at higher strain rates is usually classified according to two different mechanisms named *transition* and *shock* deformation modes [15,24]. In both cases, the deformation originates from the impact front of the material regardless of the position of its weakest section (differentiating the dynamic from quasi-static deformation). The transition mode occurs at intermediate loading velocities and deformation is restricted to the vicinity of the impact area. As a result, the average sample strain does not reach the densification strain [15,24]. Shock mode is associated with higher loading velocities. In this mode, the material deforms until the densification strain is reached [15,24].

3.3.1. Dynamic impact from EP layer

Fig. 7 shows the deformation pictures of an EP-55 sample. The deformation starts within the EP layer (impact end) and progresses up to $\varepsilon \approx 0.08$ (see also their stress-strain curves in Fig. 5). The small plateau region in their stress-strain curves further confirms the partial deformation of EP layer at the impact front (see Figs. 5 and 7). According to Refs. [15,24] the deformation mechanism of these samples is classified as the *transition* mode. The deformation of the EP-55 samples is limited to the impact end (EP layer) of the FG-MSF. No significant deformation is observed outside this region and the FG-MSF does not reach its densification strain. Therefore, this deformation behaviour can be classified as transition [15,24].

The deformation of an EP-175 is shown in Fig. 8. As can be seen, the deformation of the FG-MSF is mostly concentrated on its impact end. The compression progresses up to higher average strain values ($\varepsilon \approx 0.27 - 0.3$). The deformation pictures shown in Fig. 8 confirm the compression of the EP layer in the plateau region seen in Fig. 5. The densification of the EP layer in Fig. 8 also coincides with a stress rise at the end of the plateau region at $\varepsilon \approx 0.27 - 0.3$ (see the dashed arrow in Fig. 5). After $\varepsilon \approx 0.27 - 0.3$, a stress decline occurs in the stress-strain curves (see Fig. 5). This stress decline is associated with the formation of shear bands within the AC layer and confirms the propagation of the deformation within the material (see arrow at $\varepsilon \approx 0.31$ in Fig. 8). The stress on the samples is then arrested at $\varepsilon \approx 0.40$ (see Fig. 5). As mentioned in the previous section, at strain rates $> 2500\ s^{-1}$, the *shock deformation* mode is more pronounced [34,35] and best describes the impact behaviour of EP-175 samples. In this deformation mode, compression of the metal foam starts from the impact front (regardless of the position of the weakest section) and progresses towards the rest of the material. The average strain in the shock region reaches to the densification strain [15,24].

Unlike quasi-static compression, the stress-strain curves of the EP-55 and EP-175 show a rapid stress decline immediately after reaching their maximum initial compressive stress (see Fig. 5) It indicates the brittle compression of the EP layer at higher impact velocities. As EP particles do not have a significant contribution in compression of the MSFs [20], the stress decline after the compressive strength is most likely related to the brittleness of the aluminium alloy struts under impact loading [36]. The serrations observed in the plateau region of the impacted FG-MSF samples from the EP layer also confirm the brittleness of the foam at high loading velocities (see Fig. 5). These serrations are more pronounced at 175 m/s (see Fig. 5). The dynamic compressive properties of uniform A356/EP MSFs were studied in Ref. [13]. However, due to the higher aspect ratio of the uniform MSFs considered in Ref. [13], their deformation mechanism cannot be directly compared with the deformation of the EP layers in this study. In Ref. [16], it was shown that altering the aspect ratio in FG-MSF layers changes the deformation mechanism under dynamic compressive loadings.

3.3.2. Impact loading from AC layer

Fig. 9 shows the deformation pictures of an AC-55 sample. The corresponding stress-strain curves (see Fig. 5) are similar to the compressive stress-strain curves of a brittle metal foam such as uniform AC-MSFs that was studied under quasi-static and dynamic loadings in our previous research [16].

According to Fig. 5, a stress maximum is followed by a rapid stress decline. In Fig. 9, the limited deformation of these samples to only $\varepsilon \approx 0.052$ is visible. The compression of the FG-MSF starts with the formation of a shear band at the impact front (AC layer) at ≈ 0.026 . The shearing of this layer coincides with a stress decline in the stress-strain curves at ≈ 0.026 (see Fig. 5). Up to $\varepsilon \approx 0.052$, the compression of the samples is concentrated within the AC layer and no deformation of the EP section is visible.

This is also considered as a *transition* mode [15,24] similar to the EP impacted samples at 55 m/s.

The deformation of an AC-175 sample is shown in Fig. 10.

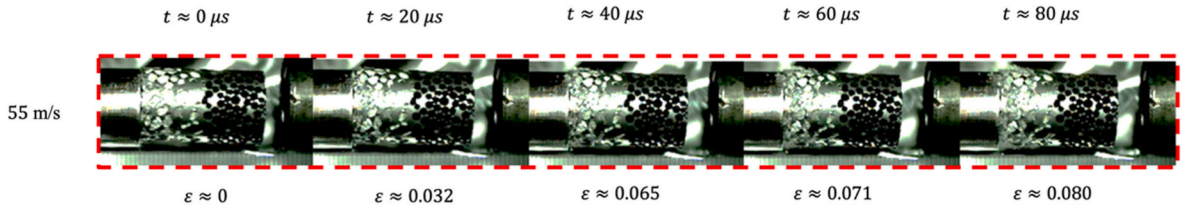

Fig. 7. Deformation of the EP-55 sample.

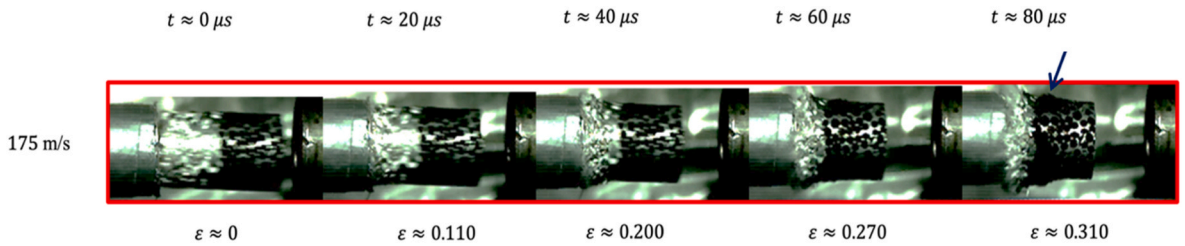

Fig. 8. Deformation of the EP-175 sample.

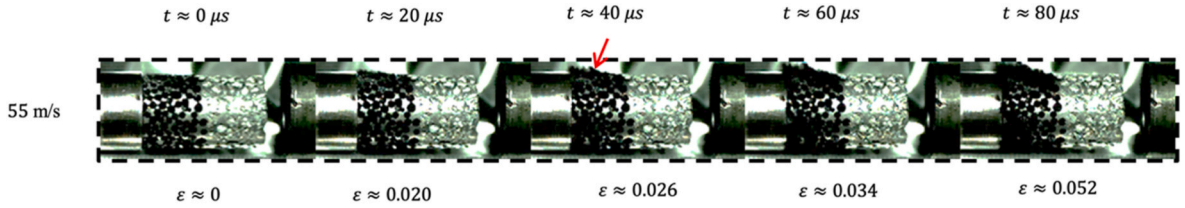

Fig. 9. Deformation of the AC-55 sample.

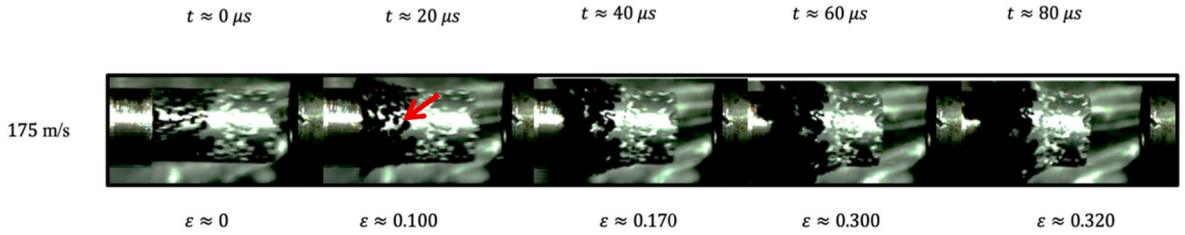

Fig. 10. Deformation of the AC-175 sample.

Deformation of the AC layer is observed in the initial stage of the impact. The stress-strain curves of these samples in Fig. 5 shows an initial stress decline at $\varepsilon \approx 0.05$ which is most likely related to the formation of the shear bands in the AC layer (see dotted arrow in Fig. 5). A second stress decline $\varepsilon \approx 0.1$ is also related to progress of shear fractures within the AC layer (see deformation of the AC layer at $\varepsilon \approx 0.1$). The onset of deformation in the EP section is also visible and highlighted by the arrow in Fig. 10. Further deformation of the AC-175 is progressed by compression of both layers after $\varepsilon \approx 0.1$ (see Fig. 10). At $\varepsilon \approx 0.17$, the compression of the samples is mostly concentrated on the EP section (see Fig. 10). Therefore, the plateau region in their stress-strain curves after $\varepsilon \approx 0.2$, is mostly related to compression of this layer (see Fig. 5).

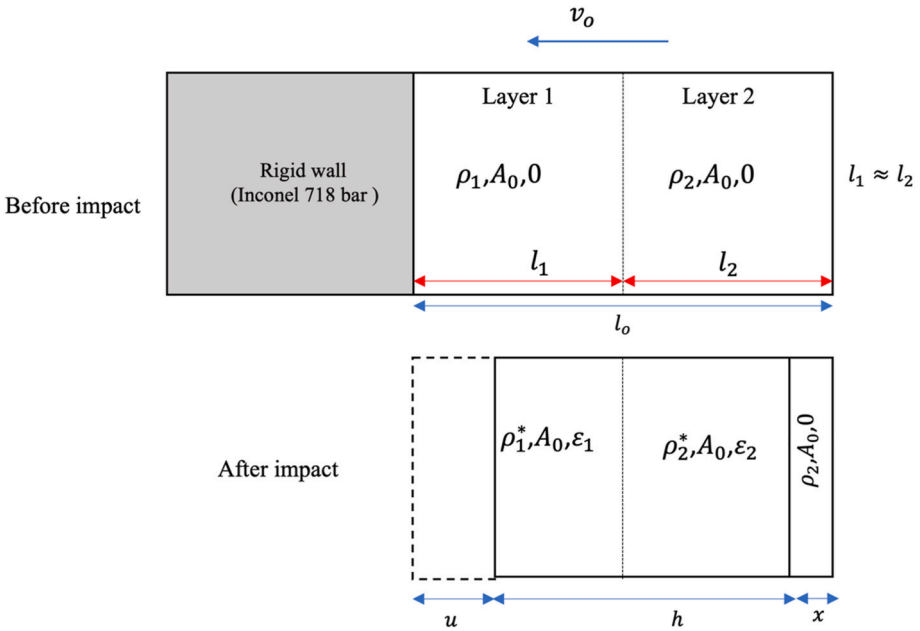

Fig. 11. Schematic deformation of the FG-MSF samples impacted at 175 m/s.

Compared to EP-175, deformation transition between layers occurs at lower average strain in AC-175 samples (see Figs. 8 and 10). In addition, for the AC-175, the initial maximum stress is considerably higher than EP-175 (see Fig. 5). This is most likely due to higher strength of the AC layer compared to the EP section. This results in a higher amount absorbed energy for the AC-175 samples in the initial stages of impact (see the areas under their stress-strain curves in Fig. 5).

In FG-MSF samples impacted at 175 m/s, shock stress occurred during densification of the impact layer. After shock stress, the partial deformation of the next layer took place with decreased strength of the EP-175 and AC-175 samples (see their stress-strain curves Fig. 5). Fig. 11 schematically shows deformation mechanism of the impacted FG-MSFs at 175 m/s. FG-MSF layers with their corresponding density ρ_i, cross sectional area A_0 and strain values ε_i are shown in Fig. 11. In this Figure, u is the displacement, h is the length of the densified region, x is the uncrushed length and l_o is the initial length that were defined in section 2.4 (the cross-sectional change is disregarded in the model shown in Fig. 11).

3.4. Mechanical properties of the FG-MSF samples

Fig. 12 is a tool that compares the mechanical properties of the FG-MSFs in different groups under different impact loading conditions. The mechanical properties of an individual group of FG-MSF within their density range also provides a guide to select a material for a specific application. Any deviation in the mechanical properties of the FG-MSFs in each group is inevitable and due to the stochastic geometry of the metallic syntactic foams.

3.4.1. Compressive proof strength

In Fig. 12a, the 1% compressive proof strength of the FG-MSF versus their density are shown. The 1% compressive proof strength quantifies the strength of a porous metal at the initial stage of its deformation at 1% average plastic strain [29]. According to Section 3.3, the dynamic deformation of FG-MSF always initiates within the impacting layer. Therefore, the 1% compressive proof strength is determined by the properties of this layer. In contrast, for quasi-static loading the 1% proof strength is governed by the compression of the weaker EP layer. As a general trend, the compressive proof strength of MSFs increases with their density that is directly proportional to the matrix volume fraction $\varnothing_M$ of the MSFs [37] (see Table 1).

As the samples in each group were selected in a narrow range of density (see Table 1), deviation in their 1% compressive proof strength is most likely due to local density variations at their impacted end. In quasi-static loading, the 1% compressive proof strength of the samples is almost identical. Quasi-static 1% compressive proof strengths exhibit the lowest values (see Fig. 11a). AC-175 show the maximum 1% compressive proof strength. The 1% compressive proof strength of FG-MSF impacting with their EP layer exhibits higher values compared to quasi-static compression. This enhanced proof strength at the higher loading velocity is most likely due to the strain rate sensitivity of the A356 matrix alloy. Contributing effects are micro-inertial effects and a possible pressure build-up of gas within the EP particles [13]. For both loading directions, the 1% compressive proof strength at 175 m/s is higher than at 55 m/s. This is most likely attributed to the strain rate sensitivity of the base A356 alloy and the micro-inertial effect. At the same loading velocity, the proof strength of FG-MSF impacting with their AC layer shows higher values compared samples impacting with their EP layer. This can be explained by the higher strength of the AC layers [16,20].

3.4.2. Plateau stress

According to ISO 13314-2011 [29], the plateau stress shown in Fig. 12b is the mean strength of metallic foams between $\varepsilon = 0.2 - 0.4$. For EP-55 and AC-55 samples, these strain levels are not reached and therefore no plateau stress could be obtained. Under quasi-static loading, the plateau strength of the FG-MSF is governed by compression of the EP layer and shows the values between the impacted samples from both layers at 175 m/s. The maximum plateau strength was observed for EP-175. The increased strength compared to quasi-static compression can be explained by dynamic strengthening of the material. Interestingly, AC-175 showed lower plateau strength compared to quasi-static compression. The deformation of samples impacting with their EP layer is mostly concentrated within this layer. The EP layer undergoes layer-by-layer deformation (see Figs. 5 and 8). In contrast, samples impacting with their AC layer undergo shear fracture resulting

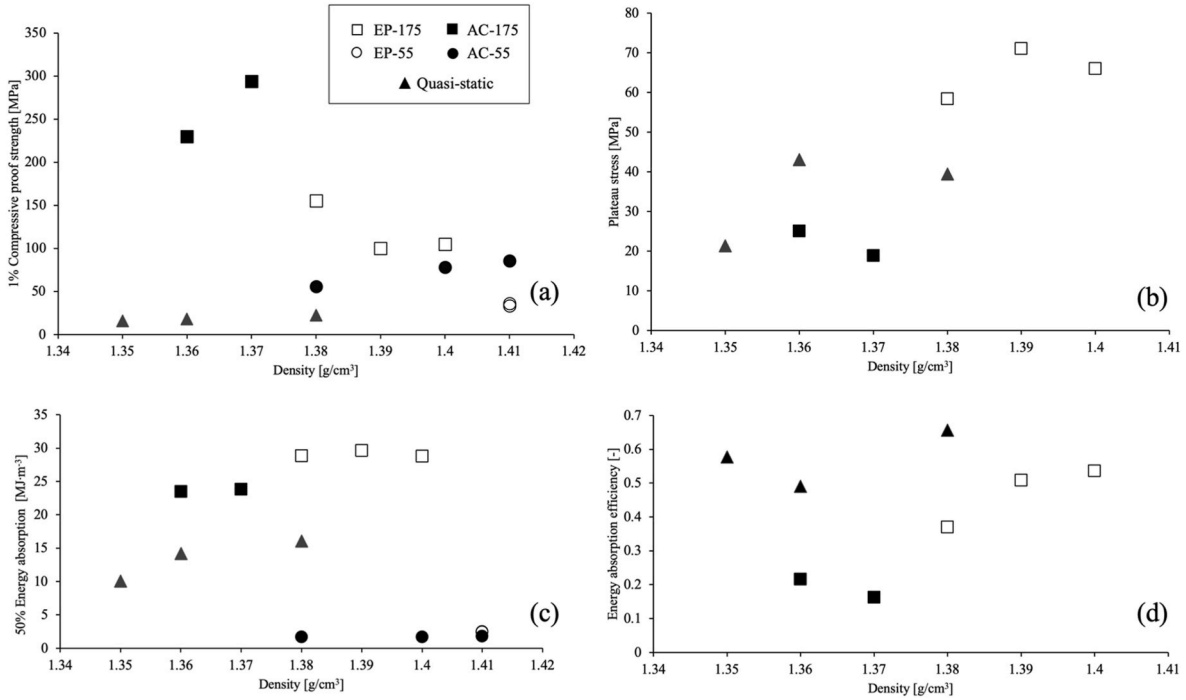

Fig. 12. Mechanical properties of the A356 FG-MSF samples under impact and quasi-static loadings.

in a decreased strength of their plateau region (see dotted arrow in Fig. 5).

3.4.3. Energy absorption

The energy absorption of the FG-MSF in Fig. 12c is calculated as the area under their stress-strain curves up to 50% of average strain according to ISO 13314-2011 [29]. The energy absorption of the metal syntactic foams usually follows the trend of the plateau strength as it captures the deformation behaviour in a similar strain interval [16]. The energy absorption of EP-175 outperforms the other sample groups. The absorbed energies of samples impacting at 55 m/s is relatively small. This is due to the low stresses and average strains recorded during their impact. Unlike the plateau stress, FG-MSF impacting with their AC layer show a higher energy absorption compared to quasi-static loading. This can be explained by the high initial stresses of AC-175 which are captured in the integration of the volumetric energy absorption but not in the calculation of the plateau stress which only considers sample's average strains above 0.2.

3.4.4. Energy absorption efficiency

The energy absorption efficiency quantifies the uniformity of the compressive stress. The energy absorption efficiency of EP-55 and AC-55 could not be calculated due to their low maximum average strains. The energy absorption efficiency for quasi-static compression is higher compared to the impacts at 175 m/s (see Fig. 12d). This is most likely due to a higher brittleness of the A356 matrix alloy at the higher loading velocity [36]. The higher brittleness of the samples at 175 m/s is further visible as considerably more serrations can be observed in their stress-strain curves (see Fig. 5). The lowest energy absorption efficiency is observed for AC-175 and can be explained by their brittle shear fracture resulting in an initial stress maximum followed by a distinct stress decline. According to Ref. [36], the increased brittleness of the A356 aluminium alloys at higher strain rates promotes foam brittleness and increases the serration within their plateau region. This consequently decreases plateau stress uniformity and energy absorption efficiency at 175 m/s. The comparison between the stress-strain curves of the FG-MSFs under quasi-static loading and those impacted at 175 m/s confirms the higher serration of the stress within the plateau regions of the impacted samples (see Fig. 5).

3.5. Comparison with r-p-p-l model

Shock deformation mode was observed for EP-175 and AC-175 samples as described in Section 3.3. For comparison, the r-p-p-l model is calculated for these groups following the procedure outlined in Section 2.4. Fig. 13 shows the obtained r-p-p-l models for the EP-175 and AC-175 samples in addition to their corresponding stress-time curves under experimental study. Comparison with experimental results provides information about the time frame that shock occurs during the impact of the metal foam. A stress decrease over time can be observed for both r-p-p-l models. For two of EP-175 samples, the calculated stress from the r-p-p-l model exceeds the experimental stress up to $t \approx 40\mu s$ (see Fig. 13a). For one of the EP-175 samples, a higher stress values compared to r-p-p-l model is also observed in the initial stages of impact between $t \approx 7 - 14\mu s$. As the density of EP-175 samples changes in a narrow range (see Table 1), this deviation is more likely due to higher local density of the impact layer in this sample. In the time range between $t \approx 40$ to $87\mu s$ the experimental stress from the impact test exceeds the calculated values from the r-p-p-l model. This time frame is associated with the densification of the EP layer (see Fig. 8) and a corresponding stress increase at $\varepsilon \approx 0.20 - 0.31$ (see Fig. 5). This indicates the existence of shock stress during this time. During the initial stage of the AC-175 impact ($t = 5$ up to $t \approx 27\mu s$), the experimental stress exhibits higher values compared to the calculated stresses of the r-p-p-l model (see Fig. 13b). During this time frame, the AC layer is deformed and also a partial deformation in the EP layer takes place (see Fig. 10). The stress rise after the initial peak is observed in their stress-strain curves at $\varepsilon \approx 0.1$ (see Fig. 5). After this time, the r-p-p-l model overpredicts the experimental stress values.

The porous EP and AC particles in the layers of FG-MSF samples were sieved in the range of 2–2.8 mm. Therefore, the polydispersity is considered negligible in these models. In addition, as described earlier, this test is a non-equilibrium test and used to determine the impact end stress. Therefore, it unfortunately cannot be used to determine strain rate dependent properties.

4. Conclusions

In this study, the quasi-static and impact loadings of A356 aluminium alloy FG-MSF samples were studied. The following main conclusions can be drawn:

- Under quasi-static compression, deformation of the FG-MSF was initially concentrated on the weaker section of the materials and then progressed towards the layer containing stronger AC particles.
- Compression of the FG-MSF started from their impact end regardless of their impact layer and velocity.
- Compression of the EP and AC layers were dominantly performed in layer-by-layer and shearing modes respectively.
- Dynamic strengthening of the FG-MSF was observed under impact loading. Increasing the loading velocity enhanced the 1% compressive proof strength and energy absorption of the FG-MSF impacted from the similar layer.

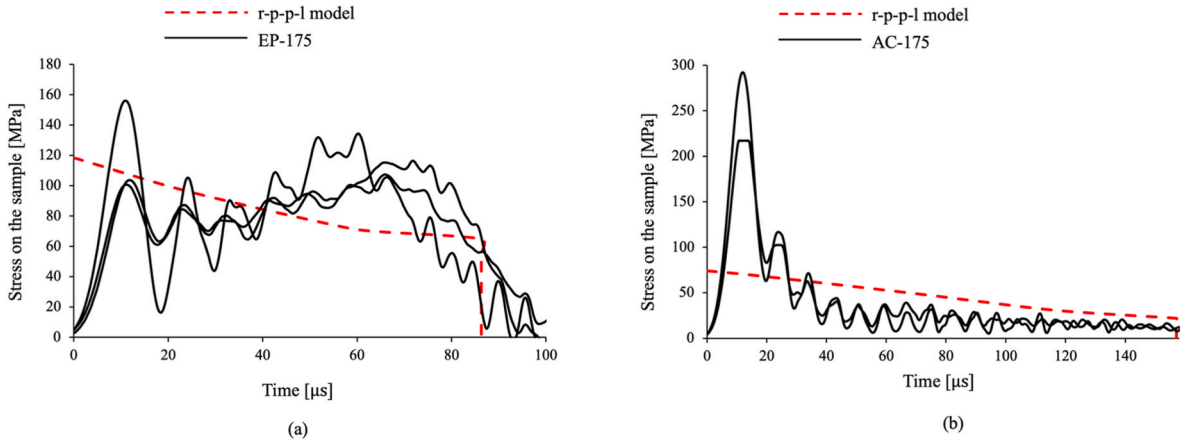

Fig. 13. The average stress-time histories of the (a) EP-175 (b) AC-175 with their corresponding r-p-p-l models.

- At similar impact velocity, the FG-MSF impacted from the AC layer showed higher strength in the initial stage of impact. While the FG-MSF impacted from the EP layer showed higher strength in the plateau region.
- Regardless of the loading direction, the transition and shock modes of deformation were observed at 55 and 175 m/s, respectively.

Data availability

The raw/processed data required to reproduce these findings cannot be shared at this time as the data also forms part of an ongoing study.

CRediT authorship contribution statement

Nima Movahedi: Conceptualization, Methodology, Investigation, Writing – original draft. **Thomas Fiedler:** Conceptualization, Methodology, Writing – review & editing, Supervision. **Alper Taşdemirci:** Investigation. **Graeme E. Murch:** Resources, Writing – review & editing. **Irina V. Belova:** Resources, Data curation. **Mustafa Güden:** Conceptualization, Methodology, Investigation, Writing – original draft, Supervision.

Declaration of competing interest

The authors declare that they have no known competing financial interests or personal relationships that could have appeared to influence the work reported in this paper.

Acknowledgement

The authors would like to acknowledge the outstanding technical support by the Univesity of Newcastle Engineering workshop and Mustafa Sarikaya and Mesut Bayhan from Dynamic Test and Modelling Laboratory of Izmir Institute of Technology for conducting the impact tests. The authors also gratefully acknowledge support by the Australian Research Council (Discovery Project Grants Scheme DP200101969).

References

[1] L.J. Gibson, M.F. Ashby Cellular Solids, Structure and Properties, Cambridge university press, 1999.
[2] N. Gupta, P.K. Rohatgi, Metal Matrix Syntactic Foams, Processing, Microstructure, Properties and Applications, DEStech Publication, Pennsylvania, 2015.
[3] E. Linul, L. Marsavina, J. Kováčik, Collapse mechanisms of metal foam matrix composites under static and dynamic loading conditions, Mater. Sci. Eng., A 690 (2017) 214–224.
[4] K. Myers, B. Katona, P. Cortes, I.N. Orbulov, Quasi-static and high strain rate response of aluminum matrix syntactic foams under compression, Compos. Appl. Sci. Manuf. 79 (2015) 82–91.
[5] A. Jung, A.D. Pullen, W.G. Proud, Strain-rate effects in Ni/Al composite metal foams from quasi-static to low-velocity impact behaviour, Compos. Appl. Sci. Manuf. 85 (2016) 1–11.
[6] S. Li, X. Guo, J. Liao, Q. Li, G. Sun, Crushing analysis and design optimization for foam-filled aluminum/CFRP hybrid tube against transverse impact, Compos. B Eng. (2020) 196.
[7] D.K. Rajak, E. Linul, Crushing response of composite metallic foams: density and high strain rate effects, J. Alloys Compd. (2021) 871.
[8] I. Duarte, M. Vesenjak, L. Krstulović-Opara, Z. Ren, Static and dynamic axial crush performance of in-situ foam-filled tubes, Compos. Struct. 124 (2015) 128–139.
[9] Y. Sun, R. Burgueño, W. Wang, I. Lee, Modeling and simulation of the quasi-static compressive behavior of Al/Cu hybrid open-cell foams, Int. J. Solid Struct. 54 (2015) 135–146.
[10] P.J. Tan, J.J. Harrigan, S.R. Reid, Inertia effects in uniaxial dynamic compression of a closed cell aluminium alloy foam, Mater. Sci. Technol. 18 (5) (2002) 480–488.
[11] M. Vesenjak, C. Veyhl, T. Fiedler, Analysis of anisotropy and strain rate sensitivity of open-cell metal foam, Mater. Sci. Eng., A 541 (2012) 105–109.
[12] M. Güden, İ. Canbaz, The effect of cell wall material strain and strain-rate hardening behaviour on the dynamic crush response of an aluminium multi-layered corrugated core, Int. J. Crashworthiness 26 (2019) 38–52.
[13] T. Fiedler, M. Taherishargh, L. Krstulović-Opara, M. Vesenjak, Dynamic compressive loading of expanded perlite/aluminum syntactic foam, Mater. Sci. Eng., A 626 (2015) 296–304.
[14] H. Lee, S. Sohn, C. Jeon, I. Jo, S.-K. Lee, S. Lee, Dynamic compression deformation behavior of SiC-particulated-reinforced A356 Al alloy matrix composites fabricated by liquid pressing process, Mater. Sci. Eng., A 680 (2017) 368–377.
[15] N. Novak, M. Vesenjak, S. Tanaka, K. Hokamoto, Z. Ren, Compressive behaviour of chiral auxetic cellular structures at different strain rates, Int. J. Impact Eng. (2020) 141.
[16] N. Movahedi, M. Vesenjak, L. Krstulović-Opara, I.V. Belova, G.E. Murch, T. Fiedler, Dynamic compression of functionally-graded metal syntactic foams, Compos. Struct. (2021) 261.
[17] J. Fan, J. Zhang, Z. Wang, Z. Li, L. Zhao, Dynamic crushing behavior of random and functionally graded metal hollow sphere foams, Mater. Sci. Eng., A 561 (2013) 352–361.
[18] S.-Y. He, Y. Zhang, G. Dai, J.-Q. Jiang, Preparation of density-graded aluminum foam, Mater. Sci. Eng., A 618 (2014) 496–499.
[19] J. Chen, P. Zhang, Y. Cheng, J. Liu, On the crushing response of the functionally graded metallic foams based on 3D Voronoi model, Thin-Walled Struct. 157 (2020).
[20] N. Movahedi, G.E. Murch, I.V. Belova, T. Fiedler, Functionally graded metal syntactic foam: fabrication and mechanical properties, Mater. Des. (2019) 168.
[21] N. Movahedi, I.N. Orbulov, A. Kemény, I.V. Belova, G.E. Murch, T. Fiedler, Fatigue characterization of functionally graded ZA27 alloy syntactic foams, Mater. Sci. Eng., A 798 (2020) 140255.
[22] T. Fiedler, N. Movahedi, L. York, S. Broxtermann, Functionally-graded metallic syntactic foams produced via particle pre-compaction, Metals 10 (3) (2020) 314.
[23] http://www.matweb.com/search/DataSheet.aspx?MatGUID=4314a54124a84c619d472a09ede7f0fe&ckck=1.
[24] M. Sarıkaya, A. Taşdemirci, M. Güden, Impact loading and modelling a multilayer aluminium corrugated/fin core: the effect of the insertion of imperfect fin layers, Strain 55 (2019).
[25] S.R. Reid, C. Peng, Dynamic uniaxial crushing of wood, Int. J. Impact Eng. 19 (5) (1997) 531–570.
[26] M. Sarıkaya, A. Taşdemirci, M. Güden, Dynamic crushing behavior of a multilayer thin-walled aluminum corrugated core: the effect of velocity and imperfection, Thin-Walled Struct. 132 (2018) 332–349.
[27] H. Anantharaman, V.C. Shunmugasamy, O.M. Strbik, N. Gupta, K. Cho, Dynamic properties of silicon carbide hollow particle filled magnesium alloy (AZ91D) matrix syntactic foams, Int. J. Impact Eng. 82 (2015) 14–24.
[28] https://imagej.nih.gov/ij/download.html.
[29] ISOMechanical Testing of Metals—Ductility Testing—Compression Test for Porous and Cellular Metals, 2011, p. 13314. Switzerland.
[30] Puat Joo Tan, Reid Stephen R, John J. Harrigan, Z. Zou, S. Li, Dynamic compressive strength properties of metal foams. PartII- 'Shock theory and comparison with experimental; data and numerical models, J. Mech. Phys. Solid. 53 (10) (2005) 2206–2230.
[31] Z. Zheng, Y. Liu, J. Yu, S.R. Reid, Dynamic crushing of cellular materials: continuum-based wave models for the transitional and shock modes, Int. J. Impact Eng. 42 (2012) 66–79.
[32] R.P. Merrett, G.S. Langdon, M.D. Theobald, The blast and impact loading of aluminium foam, Mater. Des. 44 (2013) 311–319.
[33] N. Movahedi, S. Conway, I.V. Belova, G.E. Murch, T. Fiedler, Influence of particle arrangement on the compression of functionally graded metal syntactic foams, Mater. Sci. Eng., A (2019) 764.
[34] A.T. Barnes, K. Ravi-Chandar, S. Kyriakides, S. Gaitanaros, Dynamic crushing of aluminum foams: Part I – Experiments, Int. J. Solid Struct. 51 (2014) 1631–1645.
[35] S. Lee, F. Barthelat, N. Moldovan, H.D. Espinosa, H.N.G. Wadley, Deformation rate effects on failure modes of open-cell Al foams and textile cellular materials, Int. J. Solid Struct. 43 (2006) 53–73.
[36] X. Yang, B. Zhang, Material embrittlement in high strain-rate loading, Int. J. Extreme Manufact. 1 (2019).
[37] I.N. Orbulov, A. Szlancsik, A. Kemény, D. Kincses, Compressive mechanical properties of low-cost, aluminium matrix syntactic foams, Compos. Appl. Sci. Manuf. (2020) 135.